doi:10.1017/S1431927615013379

Simulation for the Development of Electron Guns and Detection Systems of Modern Field Emission Scanning Electron Microscopes

Yoichi Ose[1], Hirofumi Sato[1], Hideo Morishita[2] and Teruo Kohashi[2]

[1.] Hitachi High-Technologies Corp., 882, Ichige, Hitachinaka, Ibaraki 312-8504, Japan.
[2.] Hitachi Ltd., Central Research Lab., 1-280, Higashi-Koigakubo, Kokubunji, Tokyo, Japan.

Introduction

The latest Field Emission (FE) Scanning Electron Microscopes (SEM) have been developed to meet the increasing demands of leading-edge users for the analysis of nanomaterials. In order to achieve optimum imaging resolution and contrast, modern SEMs incorporate innovative technologies in the FE Gun, stabilized primary electron optics, and advanced multi-detector systems for selective detection of specific electron signals. Electron optics simulators are indispensable for characterizing these functions. An axially symmetric simulator is critical for designing the primary electron optics, and a three dimensional (3D) simulator is particularly helpful for engineering and optimizing the detector system. Presented here is the theoretical basis of an axially symmetric simulator with demonstrated application results. The application and utility of a 3D simulator will also be introduced.

Theory of Electron Optics Simulation

Figure 1 shows a simulator to compute axially symmetric electric and magnetic fields (E_r, E_z, B_r, B_z) with ray traced trajectories [1,2]. These fields are governed by equations

$$\nabla(\varepsilon\nabla\phi) = -\rho \ , \tag{1}$$

$$\nabla(\nu\nabla A_\theta) + \frac{\partial\nu}{\partial r}\frac{A_\theta}{r} - \frac{\nu}{r^2}A_\theta = -J \ , \tag{2}$$

$$E_r = -\frac{\partial\phi}{\partial r}, \ E_z = -\frac{\partial\phi}{\partial z}, \ B_r = -\frac{\partial A_\theta}{\partial z}, \ B_z = \frac{1}{r}\frac{\partial(rA_\theta)}{\partial r},$$

where ϕ is the electric potential, ε is the dielectric constant, ρ is the space charge density, A_θ is the magnetic potential, ν is the reluctivity, and J is the excitation current density. The finite-difference method (FDM) is used to solve those equations. Figure 1a shows sample model geometry of an objective lens and the generated mesh. The finer mesh near the optical axis offers adequate modelling accuracy for the direct ray trace of the primary electron beam by the numerical integration of Eq. (3).

$$\ddot{\mathbf{x}} = -2\eta^2(-\nabla\phi + \dot{\mathbf{x}}\times\mathbf{B}) \tag{3}$$

Here, $\eta^2 = e/2m$ is half the specific charge of an electron. Figure 1b shows computed electron signal trajectories with both electric potential contour lines and magnetic flux lines.

Only the field data on the axis is transferred to the lens parameter simulator shown in Figure 2. Two paraxial trajectories (i.e., H and G) and aberration coefficients are calculated by solving equations as follows. The paraxial equations are

$$U'' + \frac{\Phi'}{2\Phi}U' + \frac{\Phi''}{4\Phi}U + \frac{\eta^2B^2}{4\Phi}U = 0 \tag{4}$$

$$\theta' = \frac{\eta B}{2\sqrt{\Phi}} \tag{5}$$

where $U = X + jY$ is a general paraxial ray expressed in complex form as a function of the axial coordinate z. Φ and B are the axial electric potential distribution and the axial magnetic flux density distribution respectively. The transformation between the Cartesian coordinate and the rotating coordinate is written as

$$x = X\cos\theta - Y\sin\theta$$
$$y = X\sin\theta + Y\cos\theta .$$

The formulae for computing both spherical aberration coefficient C_s and chromatic aberration coefficient C_c are

$$C_s = \frac{1}{128\sqrt{\Phi_o}}\int_{z_o}^{z_i}\sqrt{\Phi}\,[H'^2H^2\{-12S^2-16\lambda^2\} + H^4\{7S^4-8S^2S'+10S'^2+8\lambda^2S'+31\lambda^2S^2-32\lambda\zeta S+12\lambda^4+16\zeta^2\}]\mathrm{d}z \quad (6)$$

$$C_c = \sqrt{\Phi_o}\int_{z_o}^{z_i}\left(\frac{\eta^2B^2}{4\Phi^{3/2}}+\frac{3\Phi'^2}{8\Phi^{5/2}}\right)H^2\mathrm{d}z \quad (7)$$

where z_o and z_i are the object and image plane respectively, and

$$S=\frac{\Phi'}{\Phi},\quad S'=\frac{\Phi''}{\Phi}-S^2,\quad \lambda=\frac{\eta B}{\sqrt{\Phi}},\quad \zeta=\frac{\eta B'}{\sqrt{\Phi}}.$$

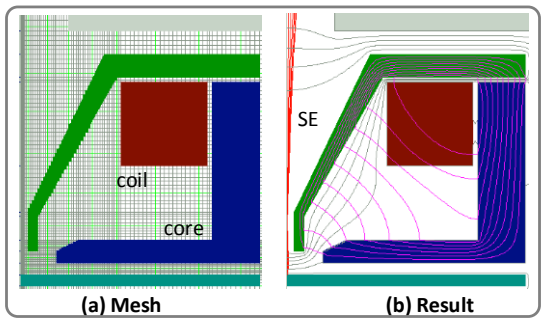

Figure 1. Axially symmetric simulator electron optics simulator based on FDM.

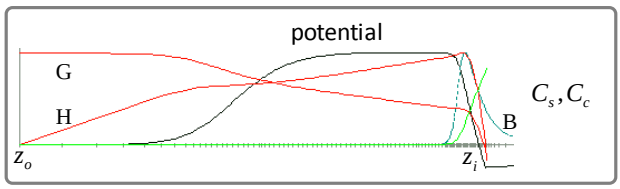

Figure 2. Lens parameter simulator calculating paraxial trajectories and aberration coefficients.

Simulation of the Electron Gun

An axially symmetric simulator for a Schottky emission gun, shown in Figure 3, has been developed using the boundary-fitted coordinate transformation method (BFM) [3], which is a variation of FDM with curvilinear mesh. The emission of electrons from a metal is a function of the temperature, electric field and work function ϕ_w [4]. The work function of the ZrO/W(100) facet surface is approximately 2.8 eV while that of the other surfaces is 4.5 eV. Angular intensity distribution of the Swanson's Schottky emission gun is analyzed and indicates good agreement with Swanson's experimental data, as shown in Figure 4 [5].

https://doi.org/10.1017/S1431927615013379 Published online by Cambridge University Press

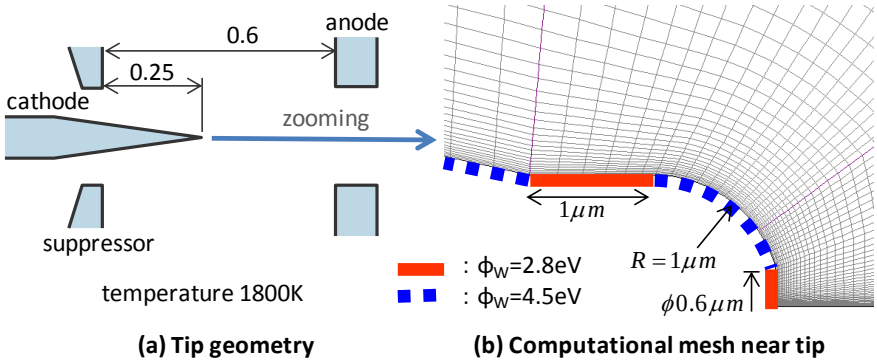

Figure 3. Schottky emission gun.

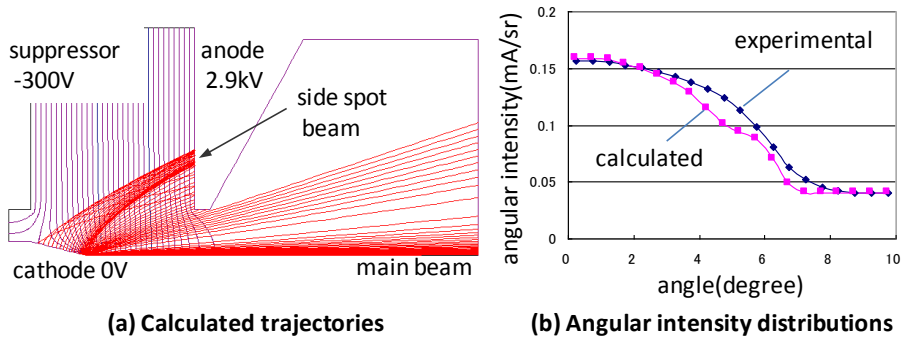

Figure 4. Verification of angular intensity distribution.

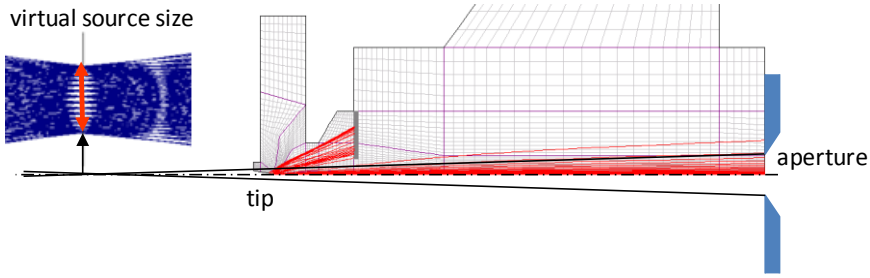

Figure 5. Estimation of virtual source size

Simulation of the multi-detector system

Figure 6 shows a multi-detector electron signal system installed in the SU8200 FE-SEM [7]. By utilizing the magnetic field generated by the Semi-in-lens, this design enables the capture of secondary electrons traveling inside of the pole-piece. Top, Upper, and Lower triple detectors offer optimum signal collection for a wide range of imaging applications. The Top detector can detect High angle BSE (HA-BSE), which has pure Z-number contrast with less topographical information. The Upper detector collects either the SE signal, for surface topography/voltage contrast, or a user-selectable low angle BSE (LA-BSE) signal for both topographical information and compositional contrast [8].

In Figure 5 a cathode virtual image and a minimum disc are obtained by interpolating the trajectory tangents from the aperture plane. The virtual sources for the spherical and facet end form cathodes are analyzed. The diameter of the minimum disc (66 nm) for the facet end form cathode is twice as large as that (32 nm) for the spherical one [6].

https://doi.org/10.1017/S1431927615013379 Published online by Cambridge University Press

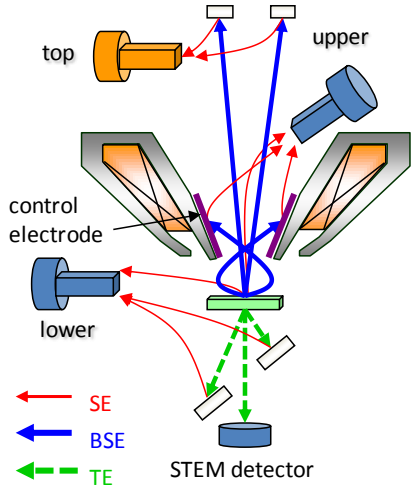

Figure 6. Multi detector system.

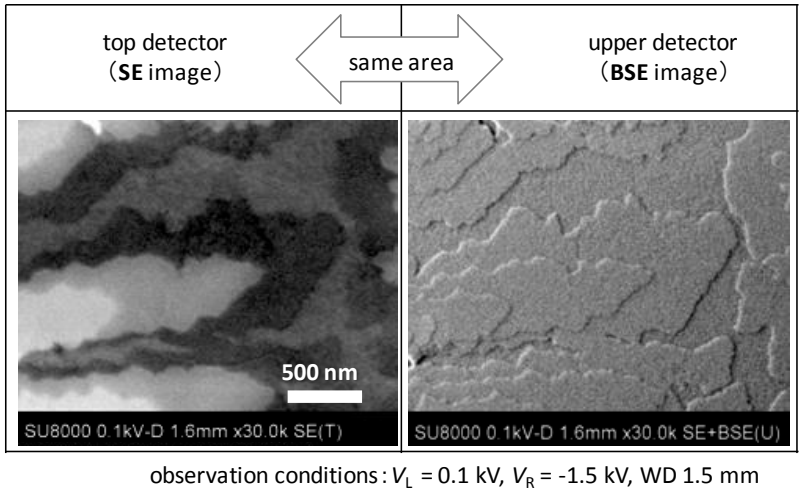

observation conditions : V_L = 0.1 kV, V_R = -1.5 kV, WD 1.5 mm

Figure 7. Contrast analysis of Pentacene thin film.

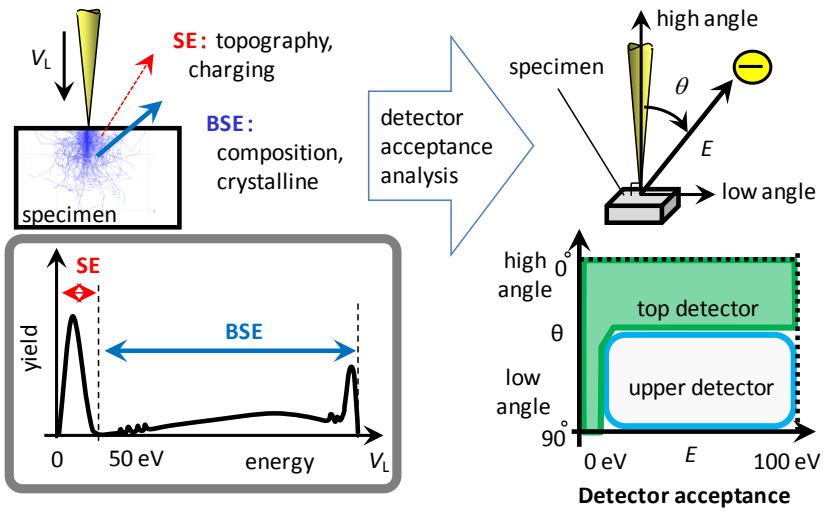

Figure 8. Specimen information included in signal electrons with specific energy and angle.

https://doi.org/10.1017/S1431927615013379 Published online by Cambridge University Press

Figure 7 shows the SE and BSE images at the same field of view and specimen location. The specimen is Pentacene of organic semiconductor, and a landing voltage of 100 V was used for the observation. Distinctive contrast of layers is observed from the SE image, and a step of 1.5 nm is clearly observed in the BSE image. Figure 8 illustrates contrast analysis with detection acceptance mapping of the multi-detector system. The Top detector primarily collects secondary electrons revealing layer dependent charge contrast. The Upper detector collects low angle BSE signal for nanoscale surface topographic contrast.

Simulation of spin SEM

Spin-polarized scanning electron microscopy (spin SEM) is a method to observe magnetic domains at the sample surface. The schematic configuration of the spin SEM chambers is shown in Figure 9. There are four chambers: load lock, preparation chamber, observation chamber, and spin detection chamber. An electron gun, SE collector, and secondary electron optics are installed in the observation chamber. The secondary electrons are transferred through the SE collector to the spin detection chamber, where a spin rotator and a spin polarimeter are installed [9].

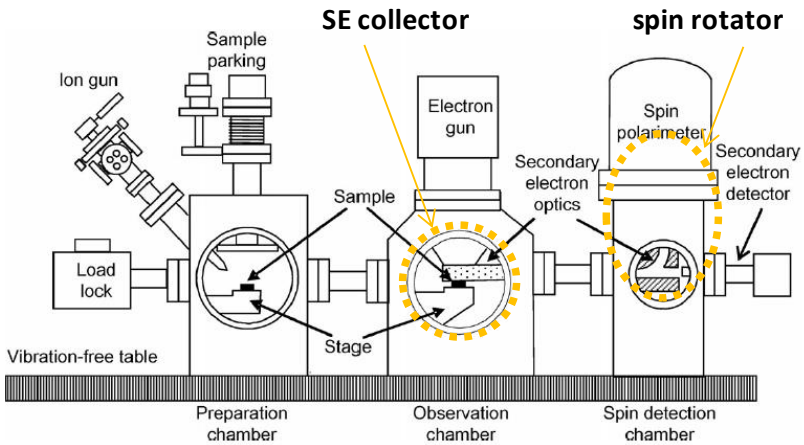

Figure 9. Configuration of spin-SEM system

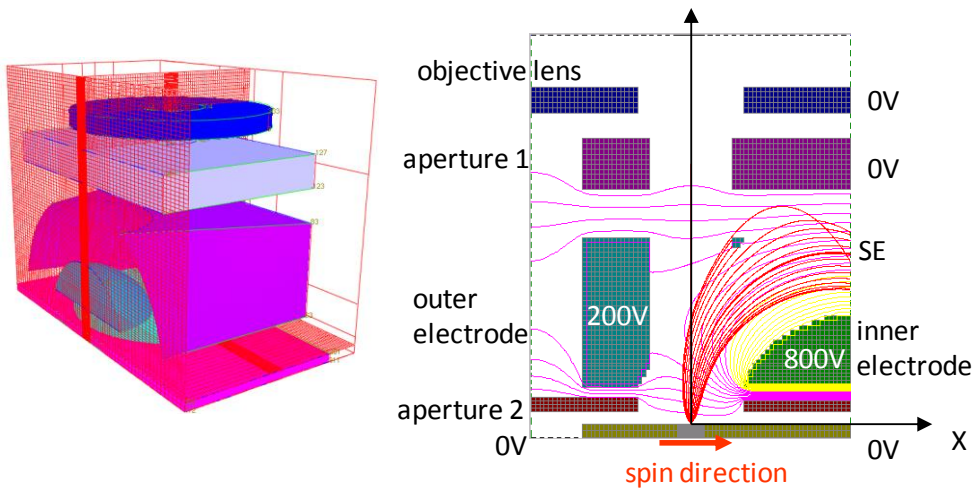

Figure 10. 3D Simulation of SE collector.

https://doi.org/10.1017/S1431927615013379 Published online by Cambridge University Press

A compact SE collector composed of an aperture and a spherical 90◦ deflector, as shown in Figure 10, was developed. This configuration was designed using the 3D simulation of the secondary electron trajectories in the electric fields. The spin rotator needs to rotate the spin-polarization vector of the electrons without changing their trajectory. A Wien filter with stigmatic focusing effect will easily accomplish this and direct electrons to the spin detector. The electric and magnetic field and electron beam trajectory were modeled using the 3D simulator in Figure 11. The important feature is the simplified structure of the spin rotator, which has no auxiliary electrodes and only requires two power supplies for the main electrodes. This design simplification was realized as a result of the 3D computer simulation [10].

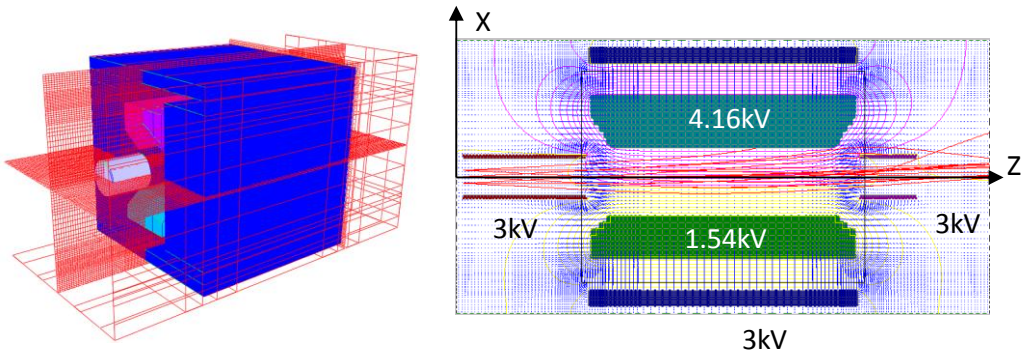

Figure 11. 3D Simulation of spin rotator.

Summary

Developed and presented here are axially symmetric and 3D simulators for electron optics and detection systems to facilitate the design of modern FE-SEMs. Each simulator offers utility for different applications. The axially symmetric simulator based on BFM was demonstrated to evaluate the virtual source size of a Schottky emission gun. This simulator, based on FDM, was also used to model and validate a multi-detector system. Additionally, the 3D simulator was indispensable in simplifying the design of the SE collector and the spin rotator of spin-SEM.

[1] Y Ose *et al*, Proc. SPIE **3677** (1999), p. 930.
[2] Y Ose *et al*, Proc. SPIE **4689** (2002), p. 128.
[3] Y Ose and K Yoshinari, Jpn. J. Ind. Appl. Math. **17** (2000), p. 357.
[4] DW Tuggle and LW Swanson, J. Vac. Sci. Technol. B **3** (1985), p. 220.
[5] LW Swanson and GA Schwind in "Handbook of Charged Particle Optics", (CRC Press, New York, 1997) p. 77.
[6] PW Hawkes and E Kasper in "Principles of Electron Optics, vol.2" (Academic, New York, 1996), Chapt. 45.
[7] S Takeuchi *et al*, Microsc. Microanal. **19** (S2) (2013), p. 1310.
[8] R Gauvin *et al*, Microsc. Microanal. **19** (S2) (2013), p. 360.
[9] T Kohashi *et al*, J. Electron Microsc. **59** (2010), p. 43.
[10] T Kohashi *et al*, Rev. Sci. Instrum. **75** (2004), p.2003.

https://doi.org/10.1017/S1431927615013379 Published online by Cambridge University Press